SSIM 2023 – PM Dight (ed.)

doi:10.36487/ACG_repo/2335_18

The importance of geological and material model detail in modelling progressive failure: Andes deep open pit

AF Puerta-Mejía *University of Alberta, Canada*

N Deisman *University of Alberta, Canada*

R Macciotta *University of Alberta, Canada*

Abstract

This study investigates the effects of geological modelling detail and material model complexity on the numerical modelling of progressive failure in deep open pit mining operations. The inter-ramp failure case is a common failure mechanism in open pit mine slopes. The research aims to identify the individual and combined effects of these factors on the precision of predicting progressive failure behaviour by systematically varying the level of detail included in the geological model and the complexity of the selected material model. The investigation aims to deepen our understanding of material model complexity and geological model detail in capturing progressive failure mechanisms. The case study demonstrates how a thorough geological model and efficient back-analysis techniques can successfully replicate observed progressive failure mechanisms, providing valuable information for infrastructure and mining industries.

The findings will offer practitioners advice on the appropriate level of complexity needed for different levels of a numerical simulation study of progressive failure. This research contributes to a better understanding of progressive failure in deep open pit mining slopes by examining the combined effects of geological model detail and material model complexity. It improves numerical modelling techniques, ultimately aiding open pit mining operations in making better safety and decision-making choices.

Keywords: *inter-ramp failure, progressive failure, rock slopes, geological modelling, material modelling, numerical modelling*

1 Introduction

Minerals are essential for modern life and are found in geologic formations at great depths. Accurate representation of progressive failure mechanisms in rock slope stability is crucial for the safety of personnel and machinery in large open pit mines while mining these minerals. Back-analysis is a powerful tool for inferring material properties from observed deformations or failures, but accurate representation requires careful consideration of geological model detail and suitable material modelling. Significant failure cases in the mining industry worldwide highlight the catastrophic effects of inadequate modelling and assessment. Knowledge about uncertainty is essential for understanding progressive failure in rock slopes, and can directly improve slope stability, resultant safety outcomes and economic benefit.

In the following sections, the paper details the site's geology, geomechanical parameters and main modelling assumptions to reproduce the failure. Onsite measurements and Google Earth satellite image analysis were used to obtain failure motion time series during the time frame. A recommended modelling workflow and results are presented, providing guidelines for analysing similar problems.

2 Case study

The back-analysis technique was applied to analyse the failure of a copper orebody exploitation in South America since 1991. The open pit, 3.9 km long, 2.7 km wide and 645 m deep, was analysed using data from the mine's operator. The mine extraction process went northwest. The initiation of a failure of the pit's northeast sector was noted in 2007 and continued as excavation progressed. The project's location on the Andes Mountain Range coincides with a geological environment with significant tectonism and thermally altered igneous lithologies. The northwest end portion of the northeast wall slope progressively failed from 2013 until complete failure in 2018. The project location can be seen in Figure 1.

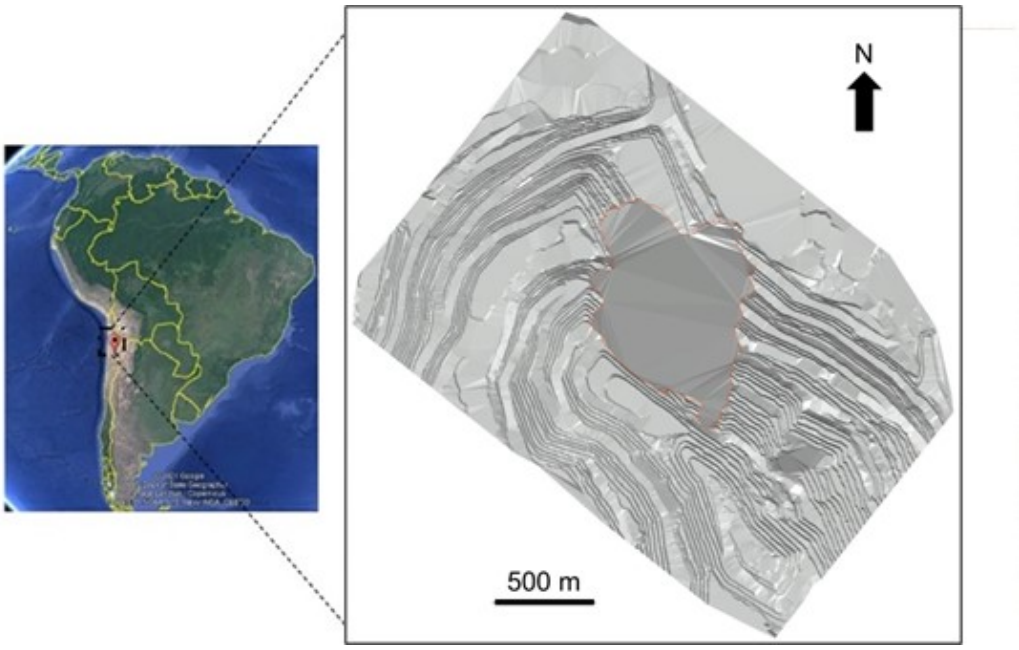

Figure 1 Project's location with failed zone plan view (modified from Google Earth)

2.1 Geological setting

The setting corresponds to a porphyry deposit where intrusive igneous bodies warm into older rocks, causing a hypothermal alteration which dominates mine geology emplaced in a subducting tectonic plate environment. High pressure or temperature from this process alters adjacent wall rock properties that control the deformation behaviour of metamorphosed rock masses. In situ features delineated in geologic and geotechnical models include rock lithology, rock mass alteration, structural setting and groundwater conditions.

2.1.1 Lithology

According to Padilla Garza et al. (2001) and Hervé et al. (2012), lithologies outcropping in the region and mine include Paleocene andesite, Paleozoic andesite (PZ), rhyolite and a quartz monzonitic-granodioritic-porphyritic stock. The stock has an elliptical shape with a maximum axis of 4.5 km long towards north 30–40° west and a minimum axis of 2.5 km. The earliest intrusion phases comprise porphyritic rocks with similar characteristics, such as phenocrysts, similar vein continuity and alteration intensity. The rhyolite has a high content of quartz phenocrysts and altered feldspar phenocrysts. Palaeocene andesite is porphyric and vesicular, contains clinopyroxene phenocrysts, and is found in a fine-grained groundmass with feldspar, biotite and minor hornblende, often with propylitic alteration. PZ is fine-grained with trachytic texture, and regionally influenced by low-grade metamorphism. Figure 2 presents the lithology distribution in the study area.

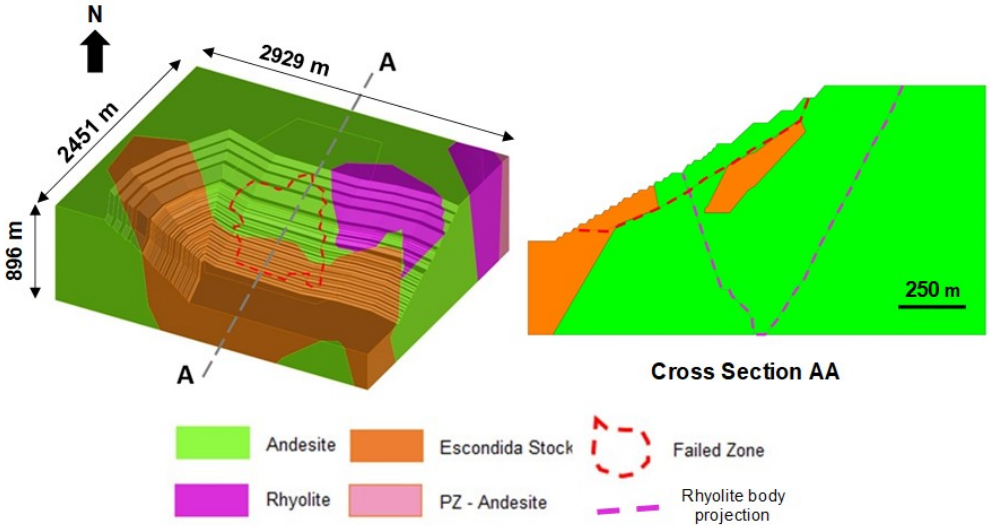

Figure 2 Isometric and cross-section views of the outcropping lithologies at the open pit failed area (built from Padilla Garza et al. 2001 descriptions)

2.1.2 Rock mass alteration

Hydrothermal alteration significantly changes minerals in rocks, with various types of altered rock masses at the mine. These alteration types include argillitic, sericitic-chloritic, propylitic, quartzite-sericitic, quazitic-sericitic and potassic. Argillitic alteration affects andesite, rhyolite and the porphyry stock, while sericitic-chloritic alteration varies from predominantly chloritic to dominantly sericitic. Propylitic alteration has veins and veinlets with typical epidote, chlorite and pyrite infill. Quartz-sericite alteration has emplaced sulphides like chalcopyrite, pyrite and molybdenite within intrusive rocks, especially along fault zones.

Potassic alteration in the stock's rocks is controlled by rock mass lithology, replacing intrusive rock crystals and groundmass, and giving rocks a pink appearance. The alteration process in the andesite rocks makes them black, with occasional large plagioclase phenocrysts. Understanding hydrothermal alteration effects on rock masses is essential for the geomechanical characterisation of materials, as discussed in Rimmelin & Vallejos (2020). Figure 3 presents the hypothermal alterations distribution in the study area.

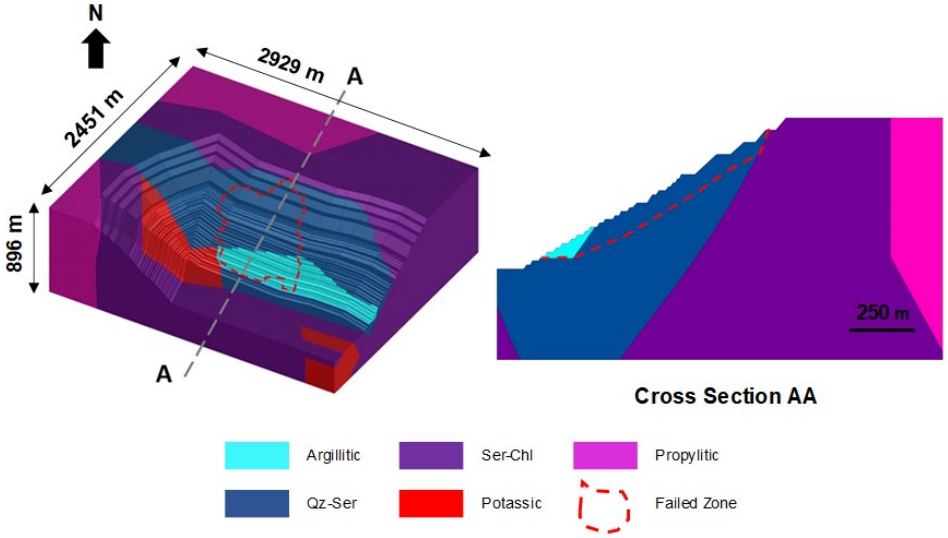

Figure 3 Isometric and cross-section views of the different alteration types at the open pit failed area (Built from Padilla Garza et al. 2001 descriptions)

2.1.3 Major structural features

Riveros et al. (2014) highlight the major fault systems in the open pit area, which have north–south, northeast–southwest, and northwest–southeast strike orientations. The north–south structure is a dextral structure that is part of the Domeyko fault system and is sealed with varying filler materials. The northeast–southwest set comprises continuous faults with an average thickness of 0.3 m and shattered zones filled with fault gouge. The northwest–southeast system is distinguished by constant wavy surfaces containing intense argillic alteration, fractured rock, fault gouge and quartz-sericite components. Table 1 presents other fault system characteristics, including persistence, thickness, filling materials, orientation (strike and dip), and relative age (order of appearance in the region). Table 2 shows slope orientation and specific fault planes with their orientation that affects the failed site.

Table 1 Major faults at mine zone characteristics (from mine's operator data 2021)

System	Relative age	Type	Mineralisation	Profile	Dip	Strike	Main infillings	Persistence	Thickness
N–S	Oldest	Strike	Yes	Wavy	70W–8E	N20W–N20E	Fractured rock or gouge	About 1 km	0.5 m
NW–SE	*Post. to N–S system	Strike	Yes	Wavy	65S–70N	N40–75W	Gouge	About 1 km	<2 m
NE–SW	Youngest	Normal	No	–	60S–70S	N60–75E	Fractured clay gouge	Greater than 2 km	0.5 m

*The relative age, post. to N–S system, indicates that the NW–SE fault system appeared after the N–S system (the first in the region) but before the NE–SW system (the youngest in the area).

Table 2 Major faults at failed zone orientations (from mine's operator data 2021)

Id	System	Dip (°)	Var. (°)	Dip direction (°)	Var. (°)
F1	NW–SE	51	±15	236	± 20
F2	NE–SW	62	±8	177	± 8
F3	NW–SE	61	±10	29	± 15
Failed slope	–	30	±5	220	± 10

2.1.4 Minor structural features

The site has minor faults and joints due to major faults movements and deformation after cooling processes. Álvarez Avendaño (2018) has presented structure sets for minor faults and joints at the mine site. Minor geological structures impacting the failed zone in terms of their dip and dip directions are listed in Table 3. The structures' persistence is lower than 100 m, which, according to the suggested scale of fault magnitude proposed by Read (2009), mainly affects the slope at a bench to inter-ramp scales.

Table 3 Minor faults and join set orientations (from Álvarez Avendaño 2018)

Minor faults				Joints			
Dip (°)	Var. (°)	Dip direction (°)	Var. (°)	Dip (°)	Var. (°)	Dip direction (°)	Var. (°)
67	±9	215	±10	65	±10	153	±10
				66	±9	214	±11
78	±5	305	±6	41	±8	188	±16
				39	±9	127	±15

2.1.5 In situ stresses

Due to the project localisation in the Andes Mountain Range, the current tectonic regime corresponds to a compressive environment. The oceanic Nazca Plate moves towards the east and is subducted under the continental South American Plate. The principal horizontal stress is expected to be oriented in the east–west direction. Padilla Garza et al. (2001) and Galarce Castro (2014) have characterised the in situ stress state within the porphyry deposit. The horizontal-to-vertical stress ratio (K) defined for the in situ model is based on mine and civil projects' stress measurements. K, at the current mine's depth range (550 m), is expected to be higher than one; for this study, K was taken as a value of 1.2.

2.1.6 Groundwater conditions

The groundwater in the open pit is heavily influenced by its proximity to the nearest recharging basin, Álvarez Avendaño (2018). The basin, a gravel aquifer laying over the andesite and rhyolite rock masses, is a recharging zone for water from anthropogenic sources like tailing dams and nearby material extraction processing plants. Once infiltrated through the overlying gravel aquifer, it is conducted to the open pit through open or fractured faults. A comprehensive drainage system has been implemented, including pumping wells, horizontal drains and a drainage tunnel system. This system has allowed the mine to maintain the water table levels before and after the failure. Consequently, the water table is below the failed zone slip surface toe; hence, the model is considered dry for this study.

2.2 Materials geomechanical parameters and geotechnical model

Data mainly comes from feasibility and early operation stages, with shear strength and deformational behaviour parameters obtained near this case study area, such as Rapiman & Sepulveda (2006) and Valdivia & Lorig (2001). Other model parameters are derived from geological descriptions and engineering judgments, like those from Lorig & Varona (2013) and Rimmelin & Vallejos (2020). The geotechnical model of rock mass lithologies and alteration states is presented in Figure 4, while the starting point for strength and deformational materials parameters are shown in Tables 4 and 5, respectively. PZ parameters were considered slightly weaker and more deformable than the Paleocene andesite; this for being the first older and more exposed to regional tectonism than the PZ andesite.

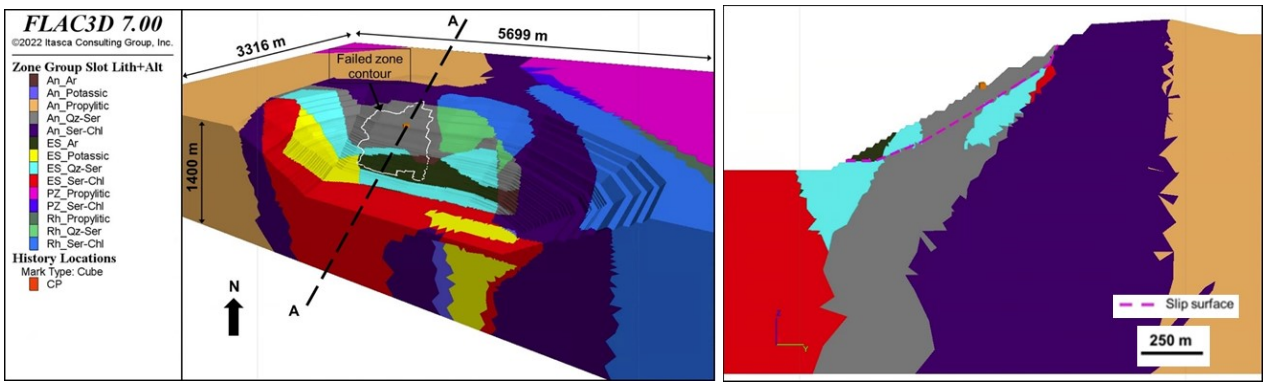

(a) (b)

Figure 4 Lithological and hydrothermal alteration distribution. (a) Isometrical view; (b) Profile view

Table 4 Mine site outcropping materials rock mass shear strength parameters

Lith.	Alt.	γ (kN/m³)		ϕ (P) (°)		C (kPa)		ψ (°)	
		Avg.	Std Dev.	Avg.	Std Dev.	Avg.	Std Dev.	Avg.	Std Dev.
Andesite (An)	Argillic	21	0	34	4	439	97	16	5
	K-Bt	25	0	38	2	537	32	23	2
	Qz-Ser	25	0	40	4	535	113	23	3
	Ser-Chl	25	–	30	–	435	–	15	–
Porphyry stock (ES)	Argillic	21.3	1.3	39	10	394	244	20	4
	Propylitic	25	–	38	–	526	–	20	–
	K-Bt	25.3	0.5	38	6	483	143	22	4
	Qz-Ser	25	0.1	39	4	506	143	23	3
	Ser-Chl	25	0	41	2	529	67	20	2
Rhyolite (Rh)	Argillic	21.3	–	43	–	1,287	–	23	–
	Propylitic	25	–	45	–	689	–	26	–
	K-Bt	26	–	37	–	840	–	21	–
	Qz-Ser	24.9	0.1	43	4	592	98	27	3
	Ser-Chl	25	–	45	–	689	–	26	–

γ: unitary weight. ϕ (P): maximum friction angle (Phi). C: cohesion. ψ: dilation angle (Dil.). argillic (Ar). Std Dev. with – symbol: only one data point; thus, the Std Dev. cannot be calculated.

Table 5 Geomechanical parameters compilation for determining mine site outcropping rock mass materials deformational behaviour, according to their lithology and alteration type

Lith.	Alt.	E_{rm} (GPa)		ν_{rm}		$\varepsilon_{\_crit}$	
		Avg.	Std Dev.	Avg.	Std Dev.	Avg.	Std Dev.
Andesite (An)	Argillic	4.2	4.6	0.27	0.01	8E-02	1E-02
	K-Bt	12.6	5.3	0.24	0.01	6E-02	7E-03
	Qz-Ser	9.9	3.9	0.24	0.01	6E-02	7E-03
	Ser-Chl	4	–	0.26	–	7E-02	–
Porphyry stock (ES)	Argillic	3.6	0.8	0.26	0	7E-02	3E-03
	Propylitic	6.1	–	0.25	–	7E-02	–
	K-Bt	11.4	6.9	0.24	0.01	6E-02	9E-03
	Qz-Ser	10.6	7	0.24	0.01	6E-02	7E-03
	Ser-Chl	4.6	1.5	0.26	0.01	7E-02	5E-03
Rhyolite (Rh)	Argillic	6.1	–	0.25	–	7E-02	–
	Propylitic	9.8	–	0.24	–	6E-02	–
	K-Bt	9.5	–	0.25	–	6E-02	–
	Qz-Ser	14.7	6.1	0.24	0.01	6E-02	8E-03
	Ser-Chl	9.8	–	0.24	–	6E-02	–

E_{rm}: rock mass deformation modulus. ν_{rm}: Poisson's ratio. $\varepsilon_{\_crit}$: plastic critical strain. Strain at which material's resistance reaches residual values, argillic (Ar).

2.3 Failure mechanism

The mine has progressed through a sequence of pushbacks in the northwest direction, with slopes facing southeast. Since 1991, unstable non-daylighting planar and wedge kinds of instability have been observed along the NE wall, some of which have progressed into high deformation/slow velocity collapse occurrences. Estimates from a Google Earth satellite image analysis completed displacement measurements for a prism in failing mass, which took measures between 2011 and 2017. Satellite images were fixed to latitude, longitude and eye altitude, and horizontal separation between failed bench edges and undisturbed positions was measured, resulting in displacement estimates. The resultant history displacement graphic illustrates three movement phases: progressive from 2004 to 2006, retrogressive from 2010 to 2013, and accelerated progressive from 2013 to 2014, using Zavodni (2009) definitions. Figure 5 presents the movement's crack evolution and displacement history plot.

The failure mechanism is considered translational, with the slip surface parallel to the slope face (30°), and the most plausible process involves rock mass shear rupture and some minor structural elements sliding. Figure 6 presents failure statistics, such as the area extension onto the slope surface, the average depth, slip surface shape and total length.

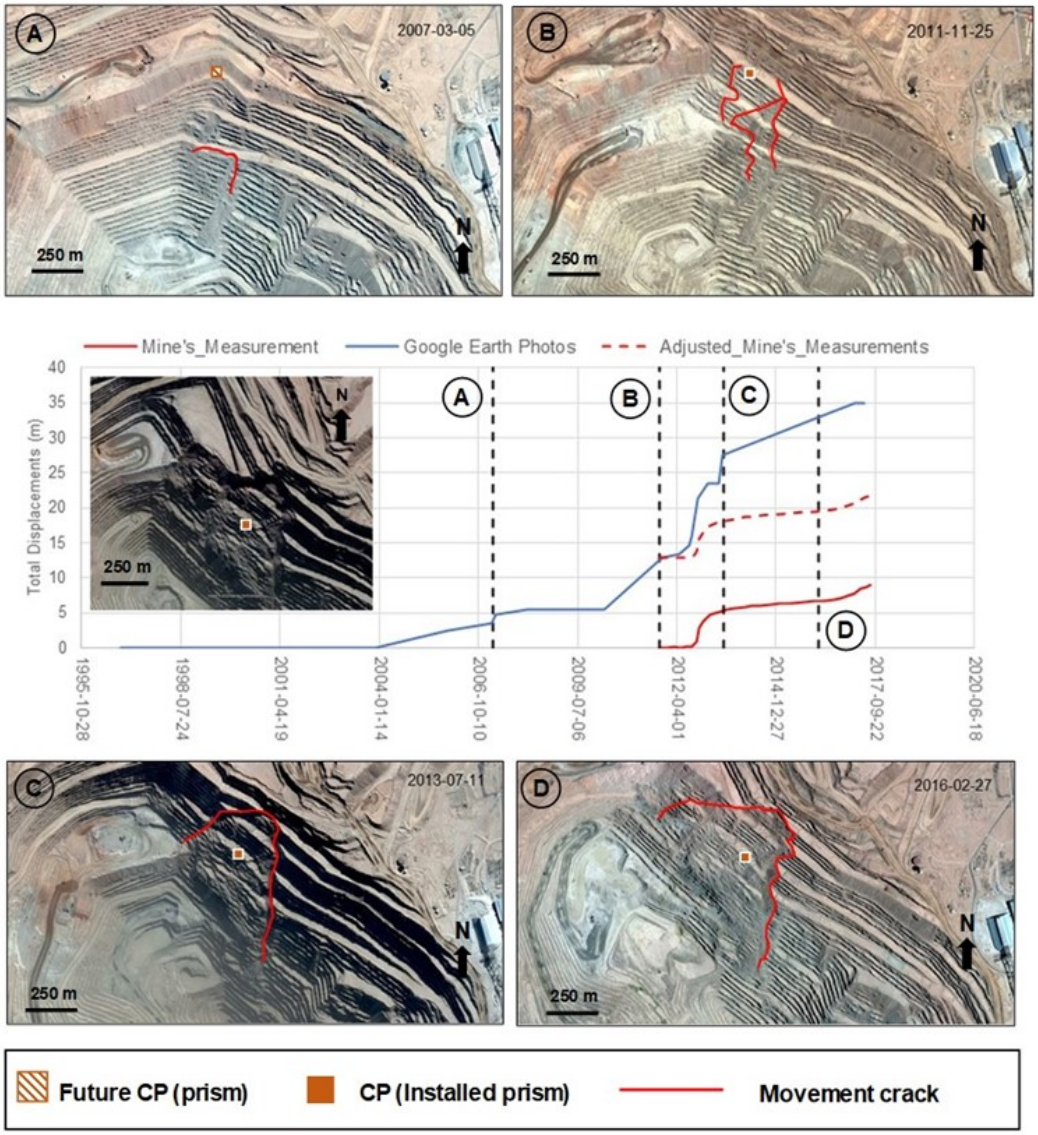

Figure 5 Cumulative displacement plot and failure extent development (from data provided by mine's operator in 2021 and imagery modified from Google Earth)

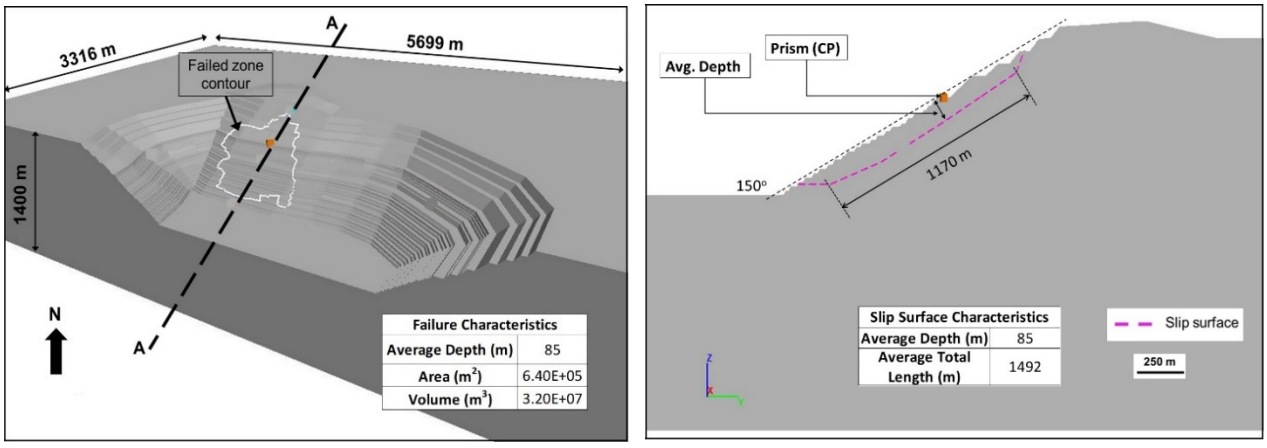

(a) (b)

Figure 6 Failure characteristics. (a) Isometric view with movement extension; (b) Cross-section A with slip surface features

3 Modelling process

Development of numerical modelling methods and codes represents the gradual increase in knowledge of materials stress-deformational behaviour and the level of complexity able to be sustained by modelling software (i.e. number of materials, spatial distribution and complexity of different geological model geometries). Material models considered for this project are linear elastic (LE), elastic perfectly plastic (EPP), and strain softening (SS). Modelled domains must account for sets of unique homogeneous materials defined by the geologically complex spatial distribution of different lithological units and the distribution of different stages of hypothermal alteration. Constitutive model effects on the models are not assessed in this work; hence, the simplest shear strength model was adopted.

The model setup involves obtaining geometrical data, operating in Rhino V. 7.0 (Robert McNeil & Associates 2020), Itasca's Rhino plug-in Griddle V. 2.0 and FLAC3D V. 7.0 software (Itasca Consulting Group, Inc. 2019a, 2019b, 2020); and setting running conditions. The model calibration process involves manually modifying material parameters. Figure 7 depicts an overview of the whole modelling process followed.

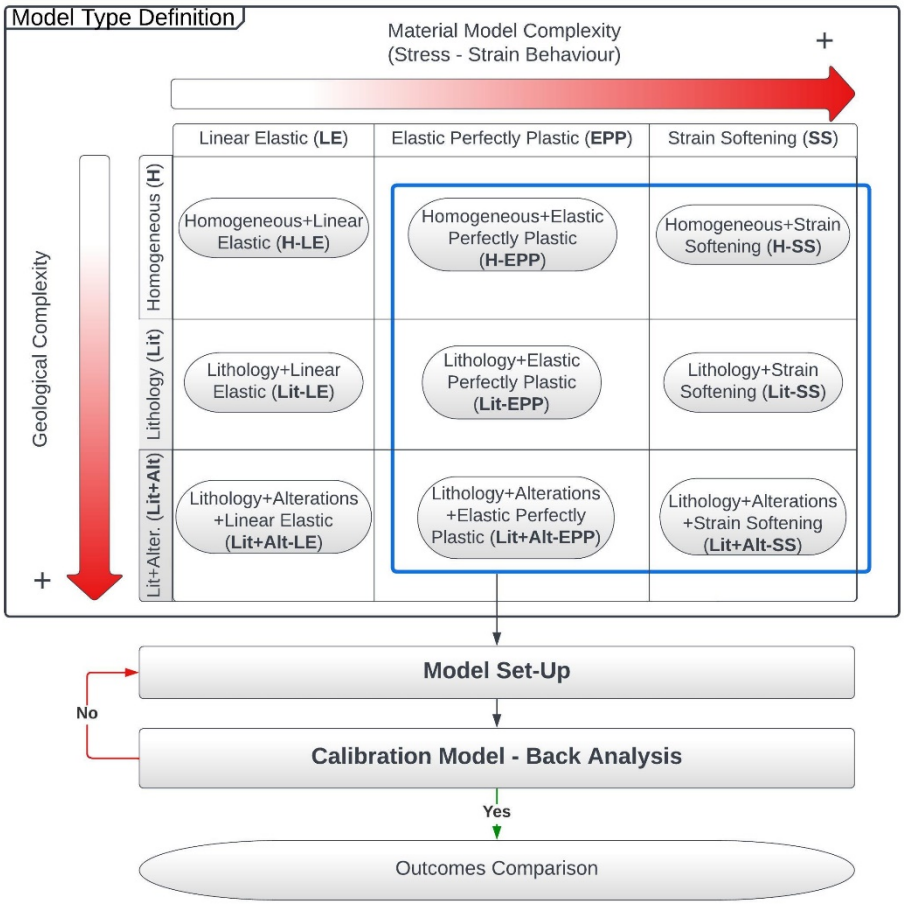

Figure 7 Flow chart showing model types for different levels of complexity and the steps involved in the overall modelling process

3.1 Model's characteristics and assumptions

The geometric model was built using Rhino V. 7.0 software, with a pushback sequence similar to the mine's actual sequencing, and focusing on reproducing lateral and vertical unloading experienced during the development of each pushback phase (Figure 8). Itasca's Griddle v2.0 and FLAC3D v7.0 software generated the meshing process and model settings. The primary model assumptions include:

- Simplified topographical features.
- Using more time-spaced data (pushbacks) at outer regions from the affected zone.
- Representing pushbacks as continuous slope faces without benching.
- Not explicitly considering major discontinuities.
- Considering minor rock mass defects implicitly in materials shear strengths.
- Not considering blasting effects on materials deformational and strength properties.
- Ensuring no interference between mechanical boundary conditions and pushback-induced stresses.

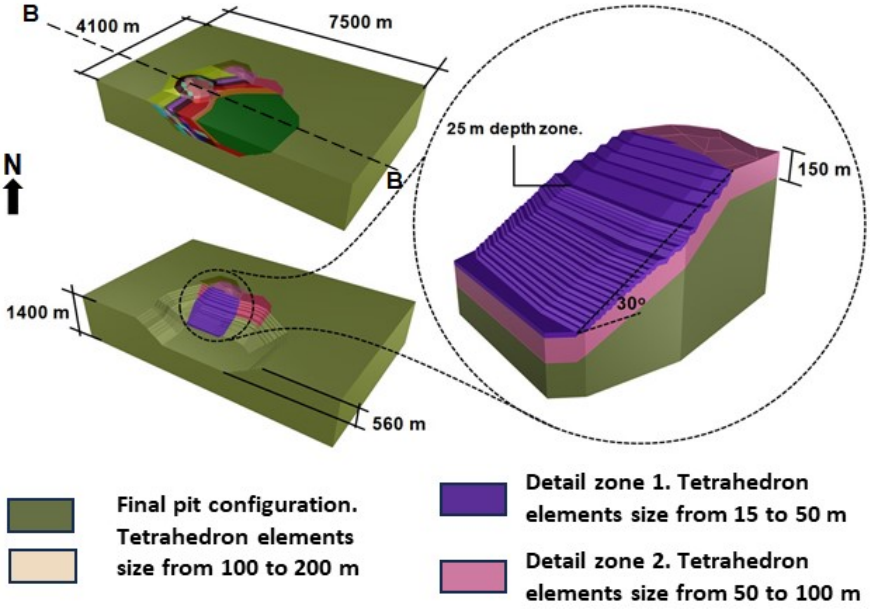

(a)

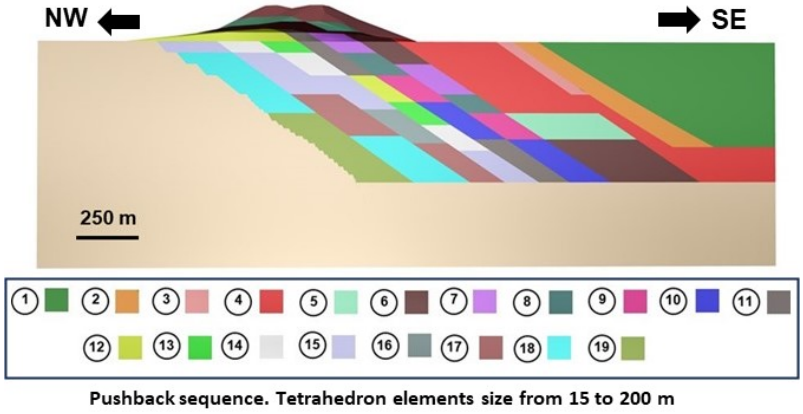

(b)

Figure 8 (a) Block model geometry, isometric views, failed zone detailing; (b) Simplified excavation sequence using Rhino V.7.0, with the size and type of elements for the mesh (modified from mine's operator data 2021)

The residual strength par1ameters were determined based on recommendations from Cai et al. (2007), with adopted values ranging between 37% and 51% of the peak values. The model running convergency criteria in FLAC3D was stable, with a range of mechanical ratios of 1e-6 to 1e-4. Models were run until convergence was achieved. The calibration criteria listed in Table 6 determined the acceptance of each model run (reflecting different levels of modelled geologic and material complexity). Model geometrical dimensions are presented in Figure 8.

Table 6 Criteria to establish when a model can be considered a calibrated model

ID	Description
C1	Either no failure or excessive displacements than at timestamp (A) from Figure 5.
C2	In the 2007 pushback, the model should show a total displacement of around 2.5 or 4.0 m in a prism located at the middle of the failed mass onto Section A, referenced in Figure 6.
C3	Once movement reaches the cumulative displacement amount and failure is indicated, maximum shear strains should end in a slip surface on section A and the affected area shape in the isometric view shown in Figure 6.

4 Results

The study shows that greater complexity models better reflect the actual failure (see Figures 9 and 10), with Lit-EPP, Lit+Alt-EPP and Lit+Alt-SS models better mimicking historical displacement (see Figure 11). The Lit+Alt-SS model comes closer to fitting the criteria because its surface area, failed volume and slip surface depth are all similar to the actual movement (see Figure 12).

A model using EPP, inclusive of the geological domains in the Lit+Alt-SS model, can reasonably reproduce some actual failure features. However, the EPP model is only accurate for estimating failure displacement timing. Lateral failure extent on the slope and displacement depth tend to be overestimated. As expected, elastic models, regardless of the lithology/alteration model applied, do not result in displacements indicating failure.

Regarding the Lit+Alt-SS model, like the other models, the back-analysis process involved a trial-and-error procedure; obtaining strength and strain parameters (C, Phi, $\varepsilon_{\_critic}$) that best characterise actual failure material behaviour. The best-fit failure model was obtained using peak shear strength parameters with peak cohesion varying from 400–700 kPa, peak friction angle between 35 and 45°, and a $\varepsilon_{\_critic}$ around 6.8E-02. Model residual shear strength values range between 40 and 60 kPa for cohesion and 20–25° frictional angle. The latter parameters classified by lithology and alteration type are presented in Table 7.

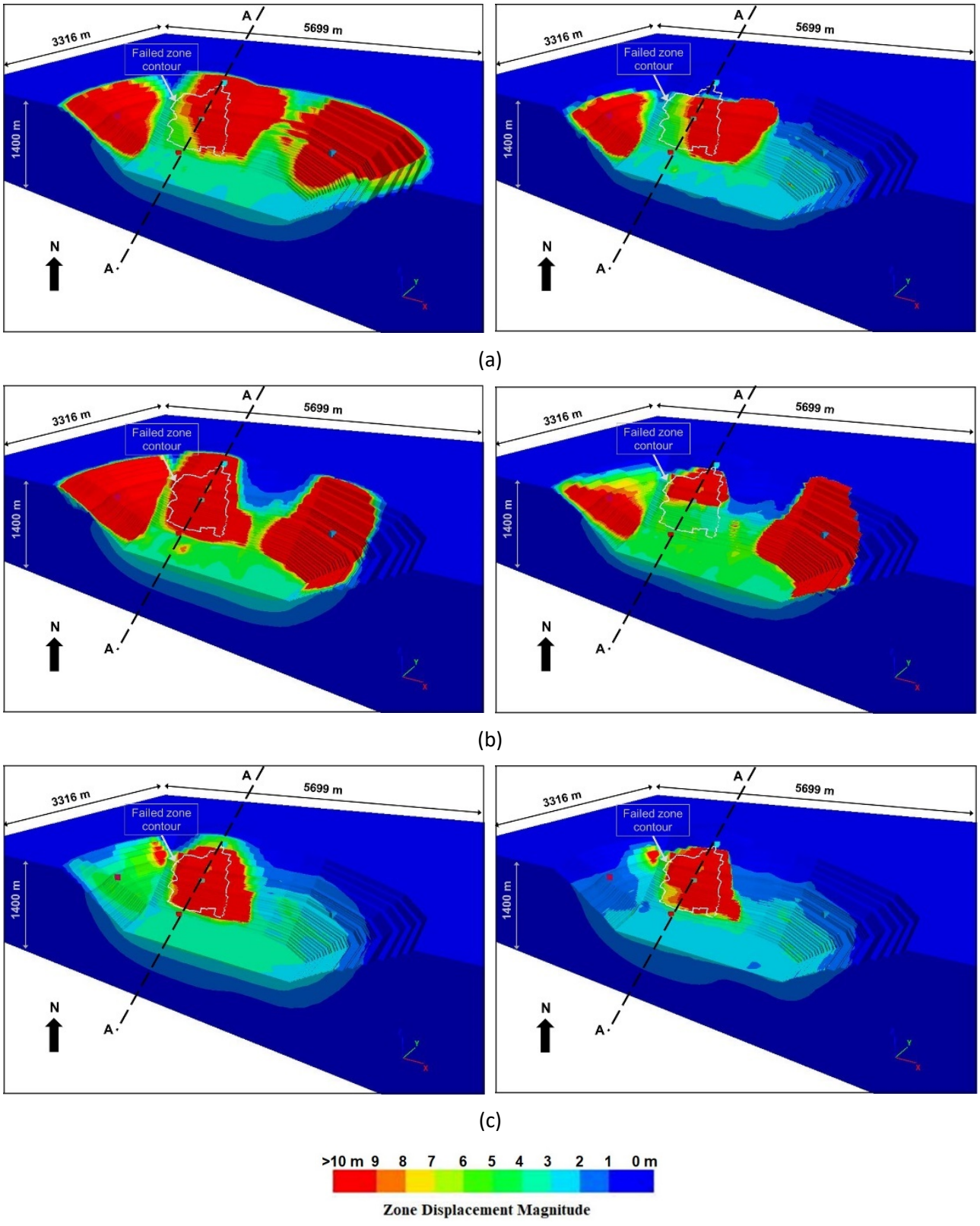

Figure 9 **Isometric views with displacement contours for the 19th pushback, comparing the different model outcomes with actual failure extent: (a) H-EPP (left) and H-SS (right); (b) Lit-EPP (left) and Lit-SS (right); (c) Lit+Alt-EPP (left) and Lit+Alt-SS (right)**

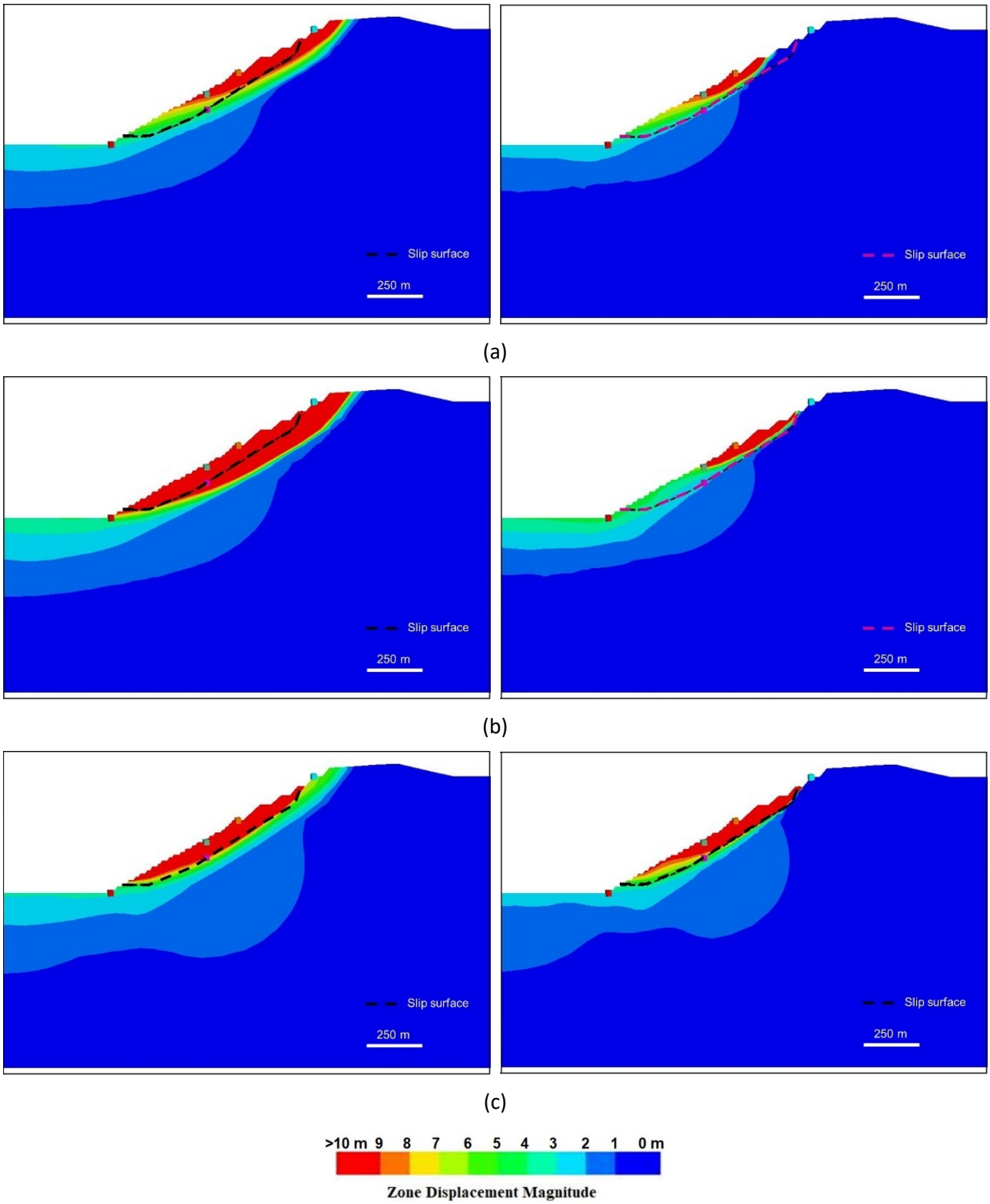

Figure 10 Cross-section (A) views with displacement contours for the 19th pushback, comparing the different model outcomes with actual failure extent: (a) H-EPP (left) and H-SS (right); (b) Lit-EPP (left) and Lit-SS (right); (c) Lit+Alt-EPP (left) and Lit+Alt-SS (right)

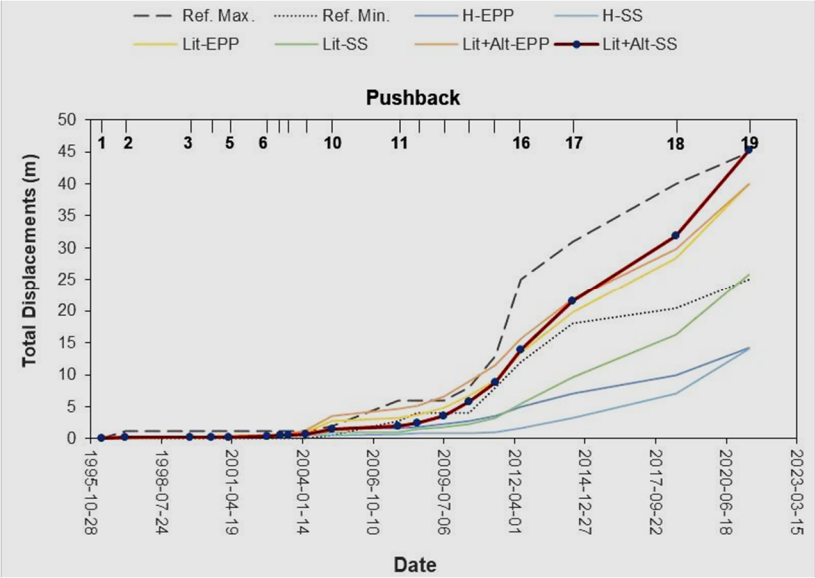

Figure 11 Obtained cumulative displacements versus time for the different model types. The adopted Lit+Alt-SS model is highlighted (bold line and timesteps)

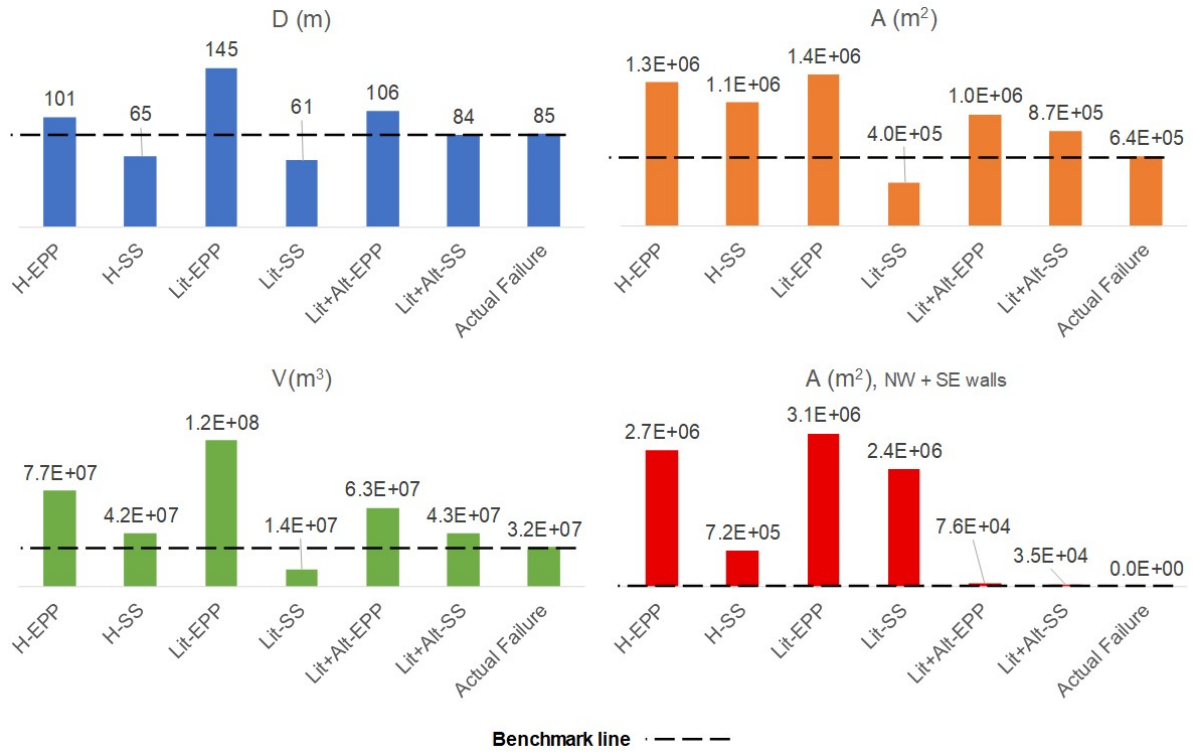

Figure 12 Bar charts comparing failure characteristics per each implemented model and the actual failure features from Figure 6

Table 7 Parameters of the Lit+Alt-SS model. Materials involved in the surface failure have an asterisk

	Peak (P)				Residual (r)					
Material	**Phi $_{(p)}$ (°)**	**C $_{(p)}$ (kPa)**	**Dil. (°)**	**$\sigma_{t\text{-}rm}$ (kPa)**	**Phi $_{(r)}$ (°)**	**C $_{(r)}$ (kPa)**	**Dil. (°)**	**$\sigma_{t\text{-}rm}$ (kPa)**	**$\varepsilon_{\_crit}$ (–)**	**$\varepsilon_{\_95\%}$ (–)**
An_Ar	34	439	17	43.9	25	40	0	10		1.0E-04
An_Potassic	38	537	19	53.7	20	40	0	10		1.0E-02
An_Propylitic	37	506	18.5	50.6	20	40	0	10	7.0E-02	1.0E-02
*An_Qz-Ser	41	612	28.7	61.2	19	40	0	10		1.0E-04
*An_Ser-Chl	38	553	19	55.3	20	40	0	10		1.0E-02
*ES_Ar	44	512	30.8	51.2	19	45	0	10		1.0E-03
ES_Potassic	38	483	19	48.3	25	60	0	10		1.0E-04
*ES_Qz-Ser	41	520	28.7	52	26	60	0	10		1.0E-04
ES_Ser-Chl	41	529	20.5	52.9	25	60	0	10		1.0E-02
PZ_Propylitic	37	506	18.5	50.6	25	60	0	10	6.6E-02	1.0E-02
PZ_Ser-Chl	38	553	19	55.3	25	60	0	10		1.0E-02
Rh_Propylitic	45	689	22.5	68.9	25	60	0	10		1.0E-02
Rh_Qz-Ser	43	592	21.5	59.2	25	60	0	10		1.0E-02
Rh_Ser-Chl	45	689	22.5	68.9	25	60	0	10		1.0E-02

Phi $_{(p)}$: peak friction angle, C $_{(p)}$: peak cohesion, Phi $_{(r)}$: residual friction angle, C $_{(r)}$: residual cohesion
Dil.: dilation angle, $\varepsilon_{\_crit}$: plastic critical strain. Strain at which material's resistance reaches residual values, $\varepsilon_{\_95\%}$: plastic strain where strength presents a 95% loss between peak and residual values.

5 Discussion

It was critical to reproduce the mine breakdown mechanism by modelling onsite lithological units, hypothermal alterations and strength-strain response. Figure 13 shows how the thorough geological model helped to confine failure extension at the slope's top (An_Ser-Chl – An_Qz-Ser contact), east and southeast (Rh_Qz-Ser – An_Qz-Ser contact), and bottom (ES_Qz-Ser – ES_Ar contact). Convexity in the northeast wall at the failure's northwest flank increases instability, however, proximity to the north wall mitigates movement on the northwest side. Figure 14 depicts lithological contacts that match with the failure slip surface, such as the vertical contact between An_Qz-Ser and An_Ser-Chl units, the stretched tabular body of ES_Qz-Ser at 85 m depth, and a sub-horizontal ES_Ar – ES_Qz-Ser material boundary at the wall's toe.

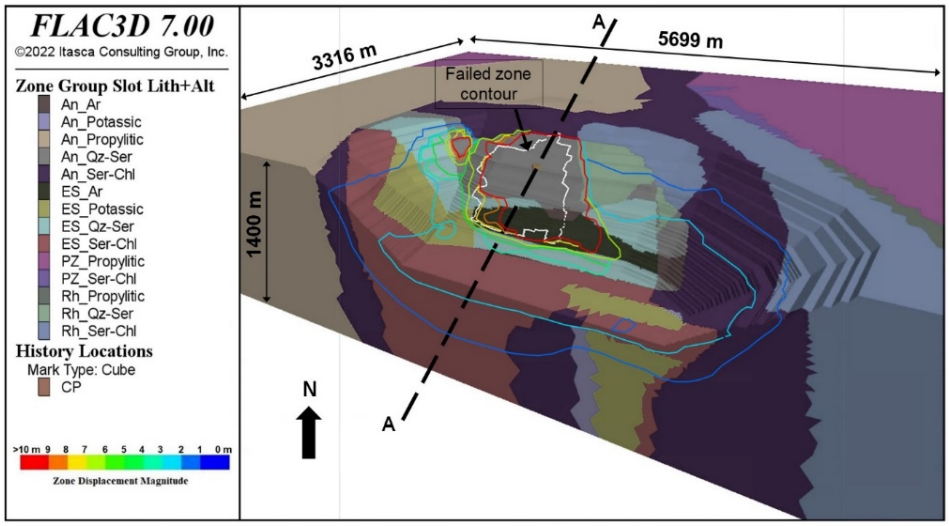

Figure 13 Isometric view showing the model's geometrical, lithologic constraint and displacement contours (modified from the FLAC3D implemented model)

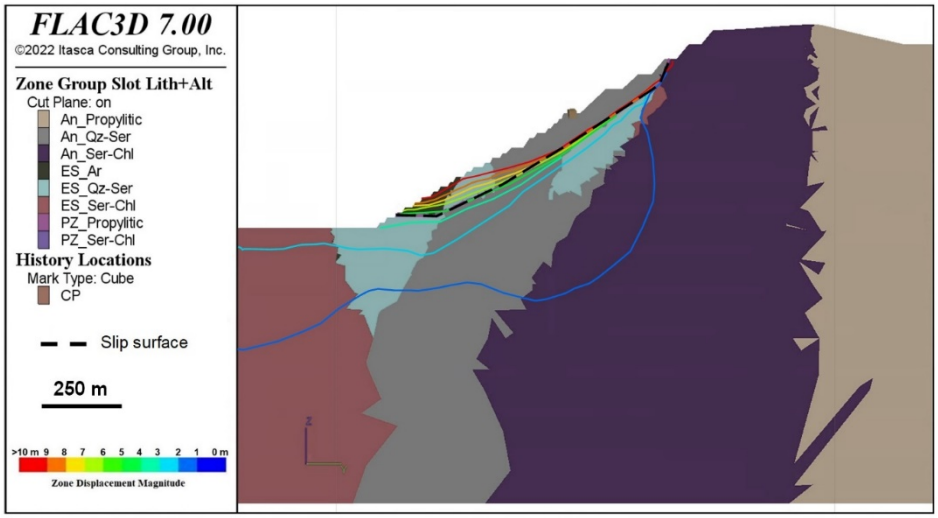

Figure 14 Cross-section with lithologic contacts and comparison with total displacement contours (modified from the FLAC3D implemented model)

The obtained outcomes showed rock mass shear strength degradation similar to previous studies using models of intact rock, rock masses with discontinuities and models with fully fractured rock mass stress-strain curves. Results are similar to those presented by Martin & Chandler (1994), Hoek & Brown (1997), Trivedi (2010) and Alejano et al. (2017).

The adopted strain softening model was essential to model the failure mechanism. Most shear strength curves reproducing the modelled deformation exhibit a bi-linear shape. An abrupt loss in shear strength (about 95%) occurs at plastic shear strains for between 1E-4 (0.01%) and 1E-2 (1%), followed by a slow reduction in shear strength before reaching residual values at around 7E-2 (7%) strains. The failure timing is closely related to excavation sequencing, shear strength curve shapes and plastic strain critical values. A higher residual friction angle contribution leads to a more surficial and stretched movement shape, while using residual cohesion values allows the deepening of the failure surface.

Although the modelled failure displacement curve shape is satisfactory and between the calibration ranges, so the results are valid (see Figure 11), found (C, Phi, ε_{crit}) values are not unique. As modelled displacements encompass a failure scenario with large cumulative deformations, the more the mesh is distorted, the higher the inaccuracy of the displacement prediction is. Hence, the final modelled cumulative displacement values

could have differed from the actual. Moreover, it is known that progressive failure modelled using strain softening is highly dependent on meshing characteristics, so especially the $\varepsilon_{\_critic}$ found in this study is not unique, as noted by Sjöberg (2009).

Linear elastic models (H-LE, Lit-LE, Lit+Alt-LE) only registered elastic rebounds as pushbacks exposed open pit walls and pit floor. Elastic rebound model deformation depends on materials deformational parameters and is proportional to the distance between the pit floor and the base of the block model extent (see Lees 2016). This type of elastic model is not capable of reproducing plastic behaviour. Hence, no signs of displacement indicating failure were observed throughout the excavation process. The more complex the geological model, the greater the overall displacements at the failure zone, as the lowest deformational moduli are concentrated at the failed location.

EPP models (H-EPP, Lit-EPP, Lit+Alt-EPP) allow a failure mechanism in the northeast wall to develop, with its extent and shape much closer to actual movement than LE models. However, EPP models are believed to present a more extensive modelled deformation response, given that strength parameters are similar to those reported for weathered soft rocks or unweathered rocks with discontinuities, such as joints with weak infill (refer to Wyllie & Mah 2017).

SS models (H-SS and Lit-SS) show an improvement of the failed zone extent as compared with the actual when combined with enhancing geological model complexity (Lit+Alt). However, as observed in section model slices, failure geometry, shape, depth of failure and sliding surface geometry still vary from the actual. In contrast, only the Lit+Alt-SS model was accurate enough to replicate failure. Overall, SS models present a shallower depth of failure and the development of intermediate failure mechanisms.

6 Conclusion

Despite advancements in field characterisation and computational techniques, there is still alarming growth in civil and mining landslide events. Reducing epistemic uncertainty can help reduce residual margins in accumulative landslide cases. Understanding materials distribution and behaviour, including key characteristics discussed in this paper, can improve back-analysis techniques and reproduce progressive failure mechanisms more accurately in infrastructure and mining industries.

This case study shows that models with more detailed or complex modelled geological domains help improve the extent and geometry of back-analysed failures compared to actual failures. The choice of a material constitutive model, such as LE, EPP or SS, also controls displacement patterns produced by the model. Based on the present study, to better represent a progressive failure mechanism, it is recommended to start with LE models, then move to EPP models and add some geological features gradually until a better simulation of failure extent is achieved, and finally move towards an SS material to match modelled slip surfaces with failure features seen in the field. This model progression method allows the modeller to check the model's numerical validity by initially employing the LE model. Homogeneous models material properties at failure are closer to residual strength values for the most detailed models. Hence they are a good starting point for more complex models. Finally, further model iterations allow adjustments to better simulate failure profile failure characteristics.

Acknowledgement

The authors express their gratitude to the people and organisations who helped this research study to be successfully completed. The authors thank the mining company for granting them access to the case study data that served as the foundation for their inquiry and The Large Open Pit project for financing this research. They also thank the academic and industrial advisors and colleagues who gave helpful advice and encouragement throughout the research process as their recommendations and knowledge were constructive in making this study a reality.

References

Alejano, LR, Arzúa, J, Bozorgzadeh, N & Harrison, JP 2017, 'Triaxial strength and deformability of intact and increasingly jointed Ggranite samples', *International Journal of Rock Mechanics and Mining Sciences*, vol. 95, pp. 87–103, https://doi.org/10.1016/j.ijrmms.2017.03.009

Álvarez Avendaño, IJ 2018, *Propuesta de Túneles de Drenaje en el Rajo Escondida y su Caracterización Geológica - Geotécnica*, PhD thesis, Universidad de Chile, Santiago.

Cai, M, Kaiser, PK, Tasaka, Y & Minami, M 2007, 'Determination of residual strength parameters of jointed rock masses using the GSI system', *International Journal of Rock Mechanics and Mining Sciences*, vol. 44, no. 2, pp. 247–265, https://doi.org/10.1016/j.ijrmms.2006.07.005

Galarce Castro, TF 2014, *Modelo de Esfuerzos in-situ para Chile y su Incidencia en el Diseño Minero Subterráneo*, bachelor's thesis, Universidad de Chile, Santiago.

Hervé, M, Sillitoe, RH, Wong, C, Fernández, P, Crignola, F, Ipinza, M & Urzúa, F 2012, 'Geologic overview of the Escondida porphyry copper district, northern Chile', in JW Hedenquist, M Harris & F Camus (eds), *Geology and Genesis of Major Copper Deposits and Districts of the World: A Tribute to Richard H. Sillitoe*, Society of Economic Geologists, pp. 55–78.

Hoek, E & Brown, ET 1997, 'Practical estimates of rock mass strength', *International Journal of Rock Mechanics and Mining Sciences*, vol. 34, no. 8, pp. 1165–1186, https://doi.org/10.1016/S1365-1609(97)80069-X

Itasca Consulting Group, Inc 2019a, *FLAC3D: Fast Lagrangian Analysis of Continua in 3 Dimensions*, computer software, Itasca Consulting Group, Inc, Minneapolis.

Itasca Consulting Group, Inc 2019b, *FLAC3D User Manual: Version 7.0*, Itasca Consulting Group, Inc, Minneapolis.

Itasca Consulting Group, Inc. 2020, *Griddle*, computer software, Itasca Consulting Group, Inc, Minneapolis.

Lees, A 2016, 'How is a geotechnical finite element analysis set up?', *Geotechnical Finite Element Analysis: A Practical Guide*, ICE Publishing, London, pp. 24–25.

Lorig, LJ & Varona, P 2013, 'Guidelines for numerical modelling of rock support for mines', in Y Potvin & B Brady (eds), *Ground Support 2013: Proceedings of the Seventh International Symposium on Ground Support in Mining and Underground Construction*, Australian Centre for Geomechanics, Perth, pp. 81–105, https://doi.org/10.36487/ACG_rep/1304_04_Lorig

Martin, CD & Chandler, NA 1994, 'The progressive fracture of Lac Du Bonnet granite', *International Journal of Rock Mechanics and Mining Sciences & Geomechanics*, vol. 31, no. 6, pp. 643–659, https://doi.org/10.1016/0148-9062(94)90005-1

Padilla Garza, RA, Spencer, RT & Pimentel, F 2001, 'Geology of the Escondida porphyry copper deposit, Antofagasta Region, Chile', *Economic Geology*, vol. 96, no. 2, pp. 307–324, https://doi.org/10.2113/gsecongeo.96.2.307

Rapiman, M & Sepulveda, R 2006, 'Slope optimisation at Escondida Norte open pit', *International Symposium on Stability of Rock Slopes*, The South African Institute of Mining and Metallurgy, Cape Town, pp. 265–278, https://www.saimm.co.za/Conferences/RockSlopes/265-278_Sepulveda.pdf

Read, J 2009, 'Structural model', in J Read & P Stacey (eds), *Guidelines for Open Pit Slope Design*, CSIRO Publishing, Collingwood, pp. 73–74.

Rimmelin, R & Vallejos, J 2020, 'Rock mass behaviour of deep mining slopes: a conceptual model and implications', in PM Dight (ed.), *Slope Stability 2020: Proceedings of the 2020 International Symposium on Slope Stability in Open Pit Mining and Civil Engineering*, Australian Centre for Geomechanics, Perth, pp. 591–608, https://doi.org/10.36487/ACG_repo/2025_36

Riveros, K, Veloso, E, Campos, E, Menzies, A & Véliz, W 2014, 'Magnetic properties related to hydrothermal alteration processes at the Escondida porphyry copper deposit, northern Chile', *Mineralium Deposita*, vol. 49, no. 6, pp. 693–707, https://doi.org/10.1007/s00126-014-0514-7

Robert McNeel & Associates 2020, *Rhinoceros 3D*, computer software, Robert McNeel & Associates, Seattle.

Sjöberg, J 2009, 'Failure mechanisms for high slopes in hard rock', in WA Hustrulid, MK McCarter & DJA Van Zyl (eds), *Slope stability in Surface Mining*, Society for Mining, Metallurgy, and Exploration, Inc, Littleton, pp. 71–80.

Trivedi, A 2010, 'Strength and dilatancy of jointed rocks with granular fill', *Acta Geotechnica*, vol. 5, no. 1, pp. 15–31, https://doi.org/10.1007/s11440-009-0095-2

Valdivia, C & Lorig, L 2009, 'Slope stability at Escondida mine', in WA Hustrulid, MK McCarter & DJA Van Zyl (eds), *Slope Stability in Surface Mining*, Society for Mining, Metallurgy, and Exploration, Inc, Littleton, pp. 153–162.

Wyllie, DC & Mah, C 2017, 'Rock strength properties and their measurement', *Rock Slope Engineering*, 4th edn, CRC Press, London, pp. 92–93.

Zavodni, ZM 2009, 'Time-dependent movements of open-pit slopes', in WA Hustrulid, MK McCarter & DJA Van Zyl (eds), *Slope Stability in Surface Mining*, Society for Mining, Metallurgy, and Exploration, Inc, Littleton, pp. 81–87.